Supplement of

The 2022 AQUAS–Tsukuba campaign: Part I. OH reactivity analysis and NO-corrected reactivity ratios for improved ozone regime evaluation

Jiaru Li et al.

Correspondence to: Jiaru Li (jiaru.li@jamstec.go.jp) and Yosuke Sakamoto (sakamoto.yosuke@nies.go.jp)

S1. Calibration experiments

LP-LIF was calibrated by measuring a known concentration of propene from a standard gas cylinder (40.4 ppmv, Sumimoto Seika Chemicals). The calibration results for total OH reactivity are shown in Fig. S1. The propene concentration was varied to establish the regression between the measured OH reactivity and the theoretic values, with each data point representing the average of 6–10 decay measurements. A rate constant of 2.6×10^{-11} cm^3 $molecule^{-1}s^{-1}$was used in the calculation (Daranlot et al., 2010). After the calibration experiments, the baseline increased by approximately 0.5 s^{-1}. The measured OH reactivity exhibited a substantial positive offset, likely caused by the zero-gas measurement, during which the mass flow controller (MFC) failed to reach the zero point for propene. Therefore, only the regression slope was used as the calibration factor. We assumed that the ambient measurement were free from offset bias based on the stable daily zero-gas measurements.

The PERCA-CAPS system consists of a polytetrafluoroethylene reactor tube (O.D 12.7 mm, and length 32cm). In the chain amplification mode, CO and NO were induced into the reactor to convert HO_2 and RO_2 radical into NO_2. In the background mode, CO was diverted to the reactor outlet, thereby suppressing the chain-amplification reactions. The difference in NO_2 concentrations measured by the CAPS instrument between the two modes, divided by the corresponding chain length, was used to derive the total HOx ($\equiv HO_2 + RO_2$) concentration. Although not all RO_2 species were quantitatively converted to NO_2 in the reactor, the system was assumed to detect the majority of ambient RO_2 radicals. The chain length was calibrated over a range of RH by measuring a known concentration of HO_2 generated via the photolysis of water vapor in the presence of excess CO. Figure S2 shows the RH dependence of the chain length used to derive ambient HOx concentrations, adapted from Sakamoto et al. (2026).

The ozone monitor, CAPS instrument, and chemiluminescence NO analyzer were calibrated after the field campaign. The calibration procedure first established the accuracy of the ozone monitor using a standard ozone generator. The calibrated ozone measurements were then used to calibrate the CAPS instrument and the NO analyzer through the titration reaction

between NO and O_3. The CO analyzer was routinely calibrated using 1.5 and 3.0 ppmv CO standard gases. In addition, canister-based measurements were used to further derive the calibration factor for ambient ground-level CO concentrations. Part of the discrepancy between online measurements and canister observations can be attributed to the different sampling heights (sixth floor versus ground level), as well as the instrumental bias. Previous studies have shown that CO concentrations may either increase or decrease with height within the urban canopy layer, depending on the surrounding building environment, before generally decreasing at higher altitudes (Rubio et al., 2008). The calibration results for the inorganic species are presented in the Fig. S3. The ozone monitor exhibited a zero-point offset, which was corrected to avoid overestimation of O_3 concentrations. In contract, both the CAPS instrument and the NO analyzer etendd to underestimate concentrations and were therefore calibrated using the corrected ozone measurements.

The VOC calibration was performed through a comprehensive comparison of online PTR-ToF-MS and GC-FID measurements with canister-based GC-FID analyses. Only VOC species that passed the calibration validation were included in the subsequent analyses. Figure S4 presents an example comparison between the online and offline measurements using isoprene. Table S1 lists the validated VOC species together with the corresponding rate constants used in the OH reactivity calculations.

S2. Observation and model results for the 2017 field campaign

Similar to the comparison presented for the 2022 field campaign, the time series of the observed and simulated OH reactivity during the 2017 field campaign are shown in Fig. S8 and S9. In contrast to the 2022 campaign, the model substantially underestimated both the total measured OH reactivity and the calculated OH reactivity (cf. Fig. 6 in Li et al., 2020). The missing OH reactivity reached up to 64% relative to the model simulation, whereas the discrepancy between the measured and calculated OH reactivity was only 35%. The largest underestimations were associated with NOx and CO (see Table 3 for daytime values and Table S2 for the entire observation period), which together accounted for approximately 18% of the total OH reactivity. Among the measured trace gases, O_3 was the only species overestimated by the model, whereas all other species were underestimated. The model underestimation was more pronounced during daytime, which may be related to insufficient representation of BVOC and OVOC emissions and chemistry.

Table S1. The list of calibrated VOCs, their average concentrations during the campaign, and their rate constants with OH.

	Concentration ± 1σ standard deviation	k_{VOC-OH} $\times 10^{-12}$ cm^3 molecule^{-1}s^{-1}
isoprene	0.35±0.24	99.6
isopentane	0.23±0.02	3.6
n-pentane	0.11±0.03	3.84
n-hexane	0.07±0.06	5.25

2,2-dimethylbutane	0.01±0.01	2.27
n-butane	0.45±0.29	2.38
benzene	0.09±0.04	1.22
propene	0.13±0.12	26
toluene	0.37±0.25	5.58
o-xylene	0.07±0.00	13.6
m,p-xylene	0.07±0.03	14.3
ethylbenzene	0.12±0.09	7
n-propylbenzene	0.03±0.01	5.8
o-ethylmethylbenzene	0.02±0.01	11.9
p,m-ethylmethylbenzene	0.04±0.01	11.8
1,3,5-TMB	0.01±0.01	56.7
1,2,3-TMB	0.01±0.00	32.7
1-butene	0.02±0.00	50.8
cis-2-butene	0.01±0.00	55.8
trans-2-butene	0.01±0.00	63.2
a-pinene	0.07±0.03	51.8
1-pentene	0.00±0.00	31.4
cis-2-pentene	0.00±0.00	65
trans-2-pentene	0.01±0.00	67
ethane	0.98±0.24	0.254
ethylene	0.48±0.04	8.15
propane	1.06±0.48	1.11
isobutane	0.28±0.20	2.14
2-methylpentane	0.08±0.02	5.2
3-methylpentane	0.05±0.01	5.2
cyclohexane	0.05±0.00	7.02
methylcyclopentane	0.03±0.00	5.68
2-methylhexane	0.01±0.00	6.89
3-methylhexane	0.03±0.00	7.17
n-heptane	0.01±0.01	6.81
methylcyclohexane	0.09±0.08	9.64
2-methylheptane	0.01±0.01	8.31

n-octane	0.01±0.00	8.16
n-nonane	0.07±0.11	9.75
n-undecane	0.02±0.01	12.3
p-diethylbenzene	0.02±0.00	16.4
m-diethylbenzene	0.03±0.00	25.5

Table S2. Comparison of the typical "trace species", total OH reactivity, and calculated OH reactivity in 2017 and 2022. The values refer to average ± 1σ standard deviation.

		NO	NO_2	O_3	CO	HCHO	k'_{total}	k'_{cal}	k'_{mdl}
		ppbv					s^{-1}		
Observation	2017	1.1±2.7	11.5±5.3	31.1±20.4	327±100	2.9±1.4	12.9±5.1	8.5±3.3	
	2022	0.14±0.27	4.3±2.1	28.3±11.2	218±43	1.3±1.1	6.0±2.5	3.3±1.1	
WRF-CMAQ	2017*	0.37±0.76	5.1±4.9	43.2±14.6	107±28	1.6±1.2			5.9±3.2
	2022^	0.46±0.93	4.6±3.1	35.9±16.7	108±29	1.0±0.5			3.4±1.4
	M2022E2017^	0.51±0.96	5.9±4.1	38.6±16.8	137±35	1.2±0.5			4.1±1.7

*2017 simulation results from 21 to 28 August. The average overall simulated OH reactivity is 4.1 ± 2.8 s^{-1} during the period of 20 August to 5 September.

^2022 simulation results from 24 August to 4 September, which is same as the OH reactivity measurement period.

Table S3. The list of reactive species from the simulation, their rate constants for modeled OH reactivity, and corresponding definition.

Species in the model	Rate coefficient in unit of cm^3 $molecule^{-1}s^{-1}$ (1E-11 means 1×10^{-11})	Definition#
NO_2	1.1E-11	Nitrogen dioxide
NO	1.04E-11	Nitric oxide
O_3	8.0823E-14	Ozone
NO_3	2E-11	Nitrate radical
HNO_3	1.5E-13	Nitric acid
HONO	6.59E-12	Nitrous acid
HO_2	1.02E-10	Hydroperoxide radical

CO	1.35614E-13	Carbon monoxide
HNO_4	4.7E-12	Peroxynitric acid
HO_2H	1.7E-12	Hydrogen peroxide
SO_2	1.3E-12	Sulfur dioxide
HCHO	8.5E-12	Formaldehyde
MEOH	9.1E-13	Methanol
CCOOOH	3.09E-14	Proposed for peroxyacetic acid
CCOOH	7.04E-13	Acetic acid.
RCOOH	1.2E-12	Higher organic acids (mechanism based on propionic acid)
RNO_3	7.2E-12	Lumped organic nitrates
ACETONE	1.91E-13	Acetone
CCHO	1.49E-11	Acetaldehyde
RCHO	3.12E-11	Lumped C3+ aldehydes (mechanism based on propionaldehyde)
MEK	5E-12	Ketones and other non-aldehyde oxygenated products which react with OH radicals faster than 5E-13 but slower than 5E-12 cm^3 $molecule^{-1}s^{-1}$. (Based on mechanism for methyl ethyl ketone).
HCOOH	3.2E-13	Formic acid
ROOH	6.8E-12	Lumped organic hydroperoxides with 2-4 carbons. Mechanism based on that estimated for n-propyl hydroperoxide.
R6OOH	1.64E-11	Lumped organic hydroperoxides with 5 or more carbons (other than those formed following OH addition to aromatic rings, which is represented separately). Mechanism based on that estimated for 3-hexyl hydroperoxide.
RAOOH	1.08E-10	Organic hydroperoxides formed following OH addition to aromatic rings, which is represented separately because of their probable role in SOA formation. Mechanism based on two isomers expected to be formed in the m-xylene system.
MGLY	1.2E-11	Methyl glyoxal
GLY	1.1E-11	Glyoxal
AFG1	3.39E-11	Lumped photoreactive monounsaturated dicarbonyl aromatic fragmentation products that photolyze to form radicals

AFG2	5E-11	Lumped photoreactive monounsaturated dicarbonyl aromatic fragmentation products that photolyze to form non-radicals
BALD	1.2E-11	Aromatic aldehydes
AFG3	7.2E-11	Lumped diunsaturated dicarbonyl aromatic fragmentation product
MACR	2.84E-11	Methacrolein
MVK	1.99E-11	Methyl vinyl ketone
HOCCHO	1.15E-11	Glycolaldehyde
ACROLEIN	1.96E-11	Acrolein
ETHENE	8.15E-12	Ethene
PROPENE	2.6E-11	Propene
BUTADIENE13	6.59E-11	1,3-butadiene
ISOPRENE	9.96E-11	Isoprene
APIN	5.18E-11	Alpha-pinene
ACETYLENE	7.56E-13	Acetylene
BENZENE	1.22E-12	Benzene
TOLUENE	5.58E-12	Toluene
MXYL	2.31E-11	M-xylene
OXYL	1.36E-11	O-xylene
PXYL	1.43E-11	P-xylene
TMBENZ124	3.25E-11	1,2,4-trimethyl benzene
ETOH	3.4E-12	Ethanol
ALK1	3.41E-13	Alkanes and other non-aromatic compounds that react only with OH, and have relatively small kOH.
ALK2	1.7E-12	Alkanes and other non-aromatic compounds that react only with OH, and have larger kOH than ALK1.
ALK3	3.41E-12	Alkanes and other non-aromatic compounds that react only with OH, and have larger kOH than ALK2.
ALK4	6.81E-12	Alkanes and other non-aromatic compounds that react only with OH, and have larger kOH than ALK3.
ALK5	6.81E-12	Alkanes and other non-aromatic compounds that react only with OH, and have larger kOH than ALK4.

OLE1	4.77E-11	Alkenes (other than ethene) with kOH no greater than 4.77E-11 cm^3 $molecule^{-1}s^{-1}$.
OLE2	4.77E-11	Alkenes with kOH above 4.77E-11 cm^3 $molecule^{-1}s^{-1}$.
ARO1	1.36E-11	Aromatics with small kOH
ARO2MN	1.36E-11	ARO2 minus naphthalene
NAPHTHAL	2.31E-11	Naphthalene
TERP	7.35E-11	Terpenes
SESQ	2E-10	Sesquiterpenes

For the details of the description of the model output, please refer to https://github.com/USEPA/CMAQ/blob/main/CCTM/src/MECHS/mechanism_information/saprc07tic_ae7i_aq/saprc07tic_ae7i_aq_species_table.md

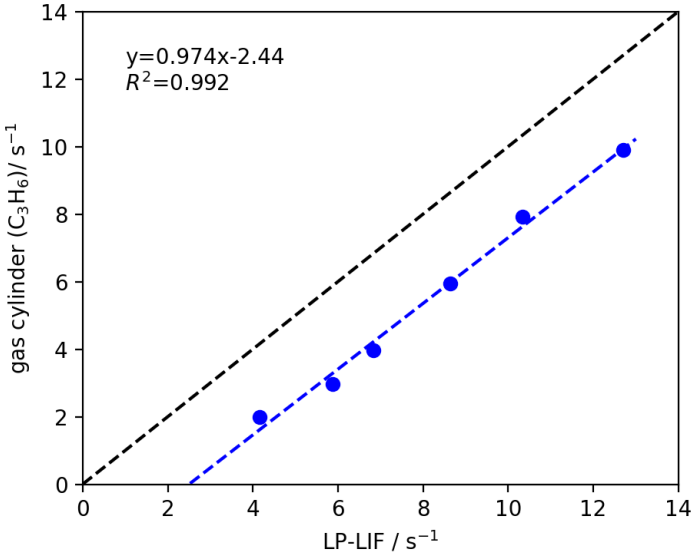

Figure S1. Calibration and regression analysis of the total OH reactivity.

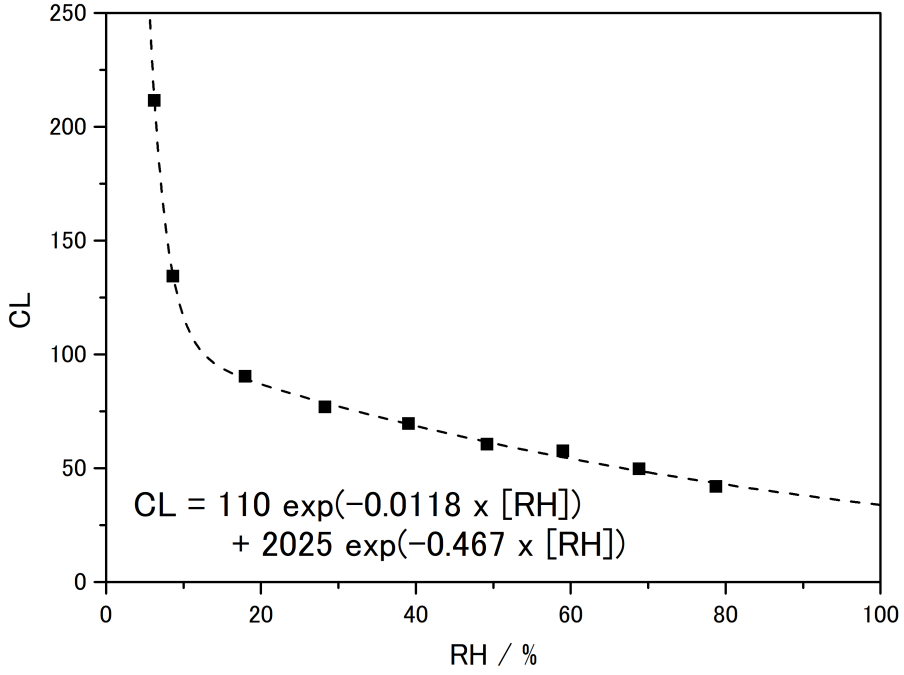

Figure S2. RH dependence of the chain length (CL) from calibration experiments conducted at room temperature (298K). Figure adapted from Sakamoto et al. (2026).

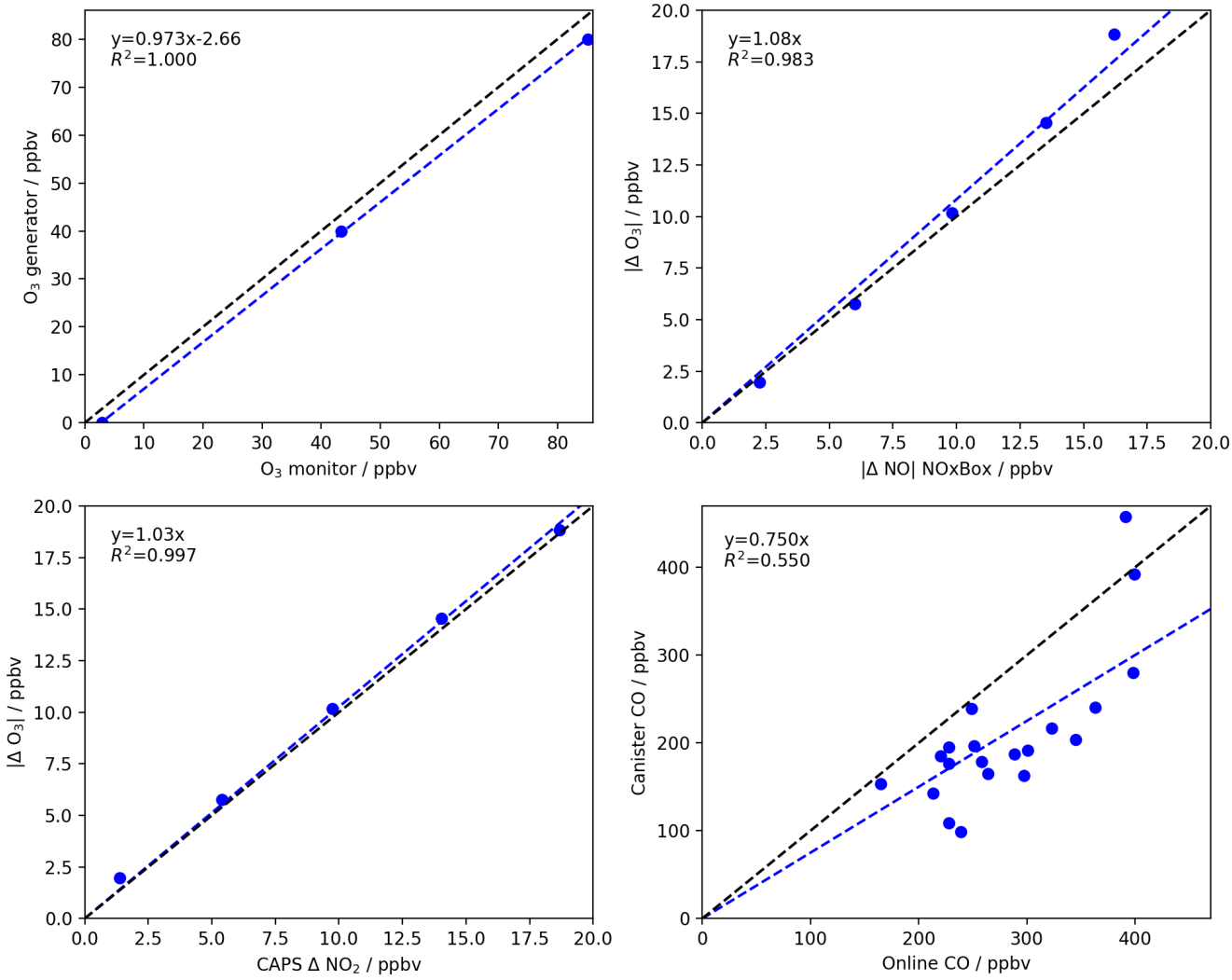

Figure S3. Calibration and regression analysis of ozone, NOx, and CO. CO concentration from online measurement was further calibrated using canister result collected at the sample time.

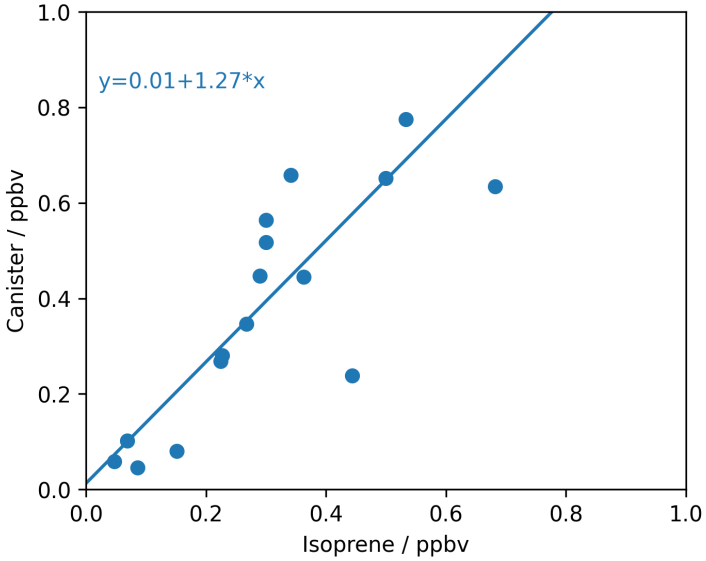

Figure S4. Cross-comparison of isoprene from the online and offline measurements.

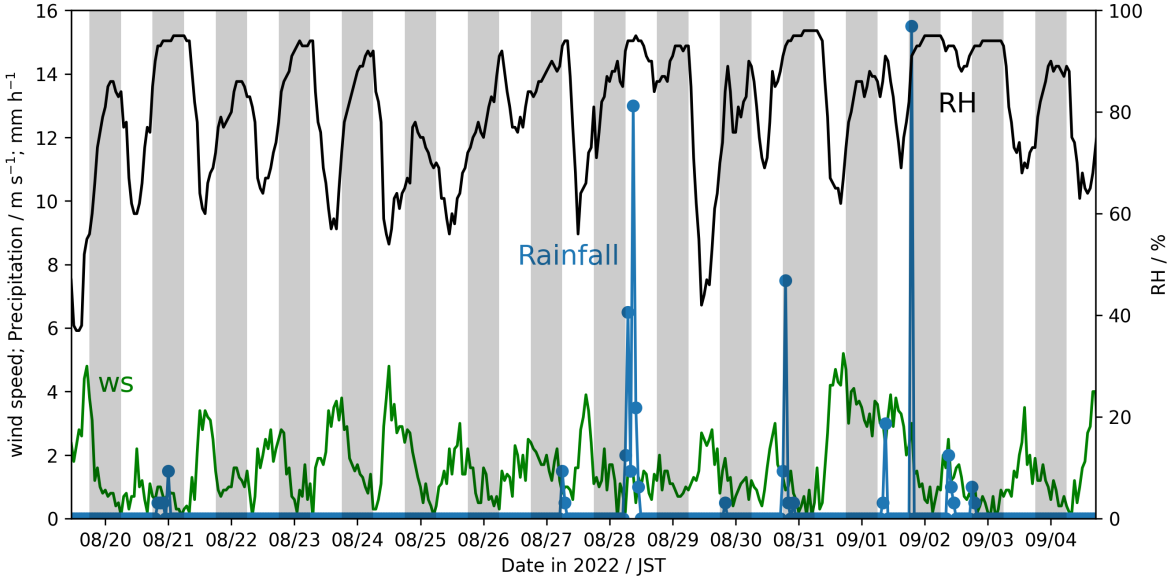

Figure S5. Time series of precipitation (in blue), wind speed (in green), and RH (in black).

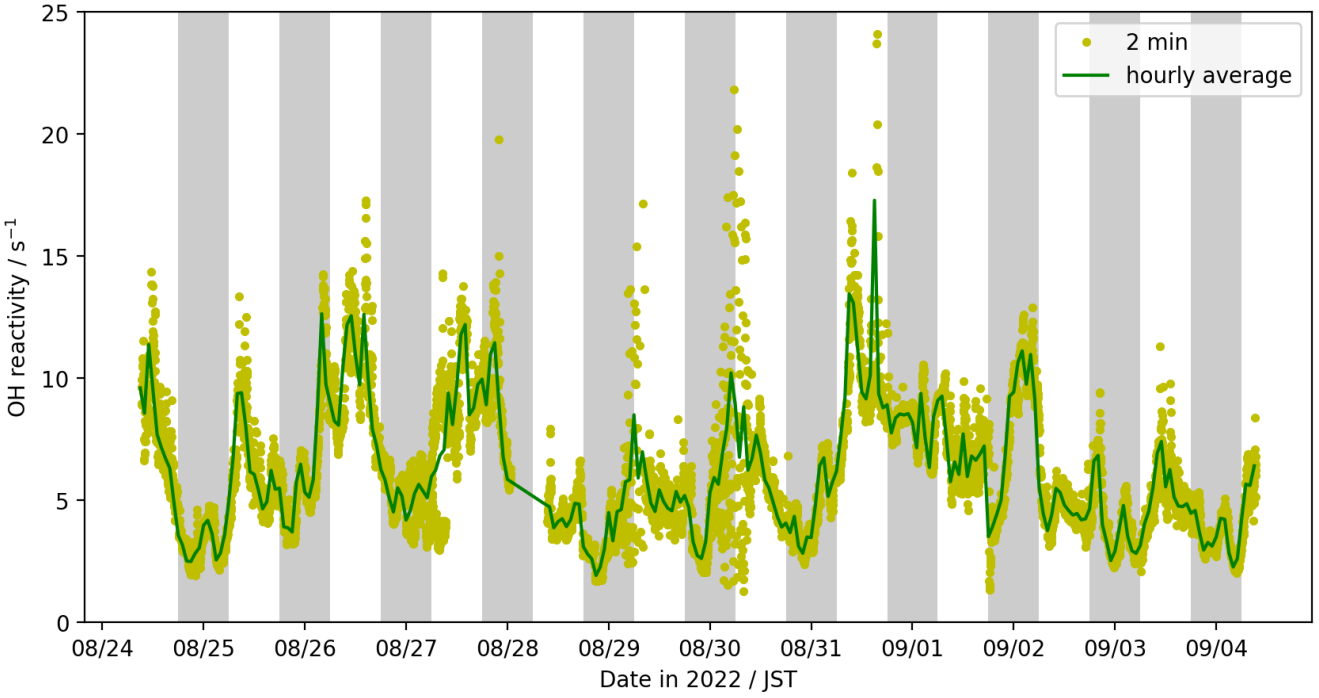

95

Figure S6. Time series of total OH reactivity from the campaign in 2–min and 1–h time resolution.

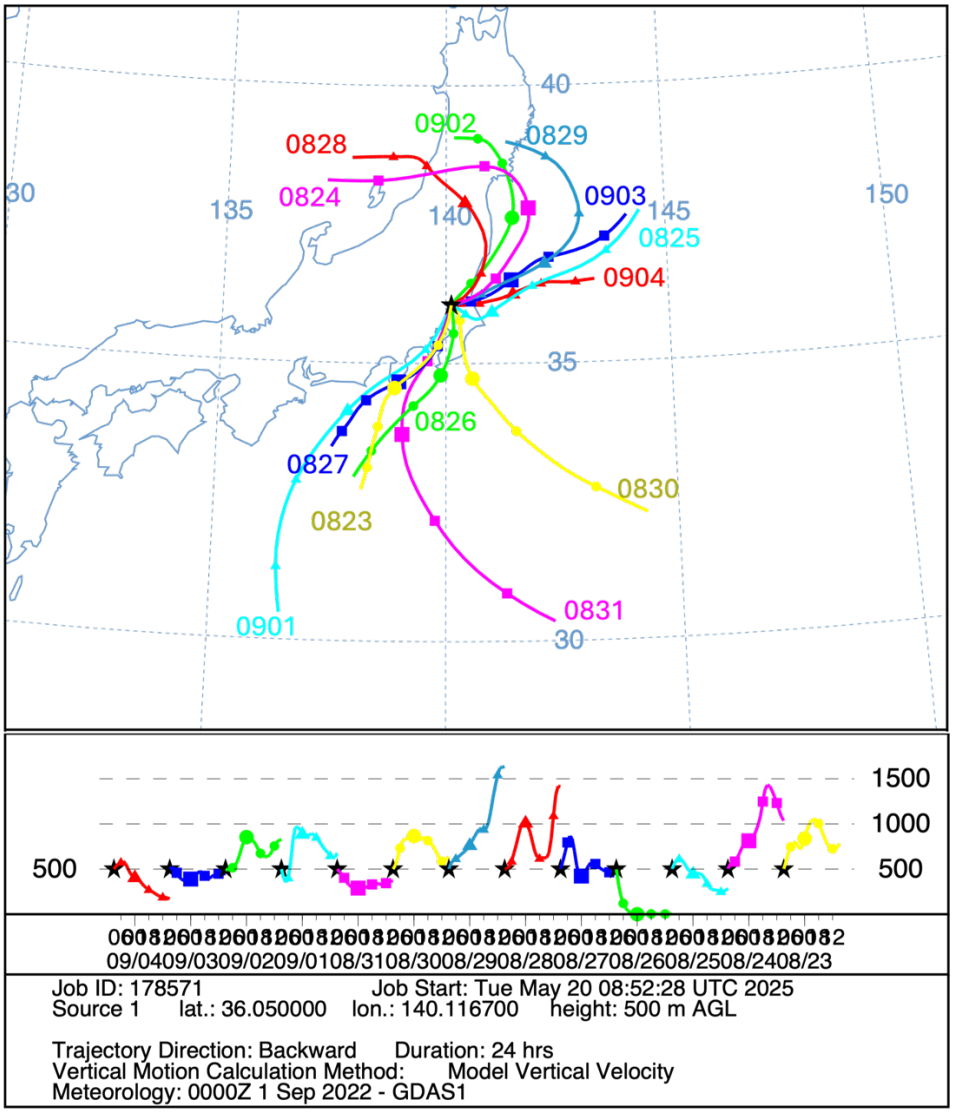

Figure S7. Backward trajectory analysis of the observation site (36.05°N, 140.12°E) ending at JST 18:00, Sep 4th at 500-meter height with a duration of 24 hours using GDAS Meteorological Data.

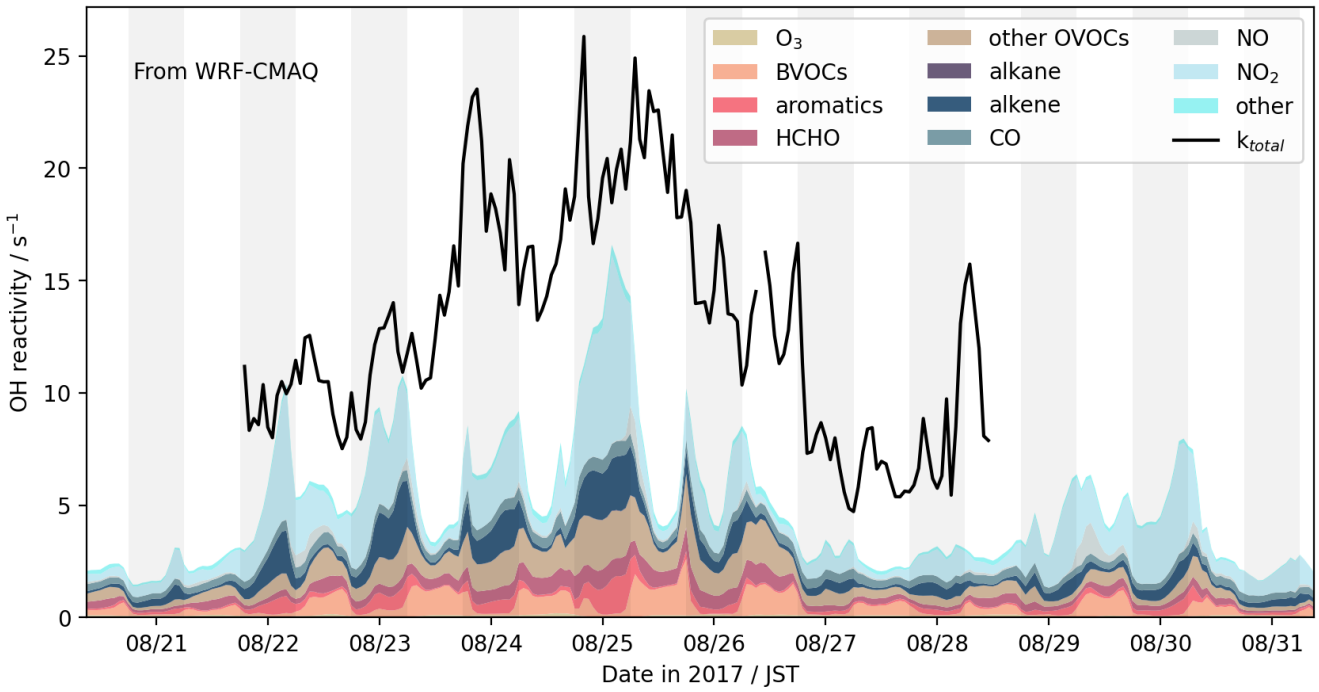

Figure S8. Hourly average of total OH reactivity (in line) and its contribution from each group of trace species (in stocked areas) based on simulation in 2017 field campaign.

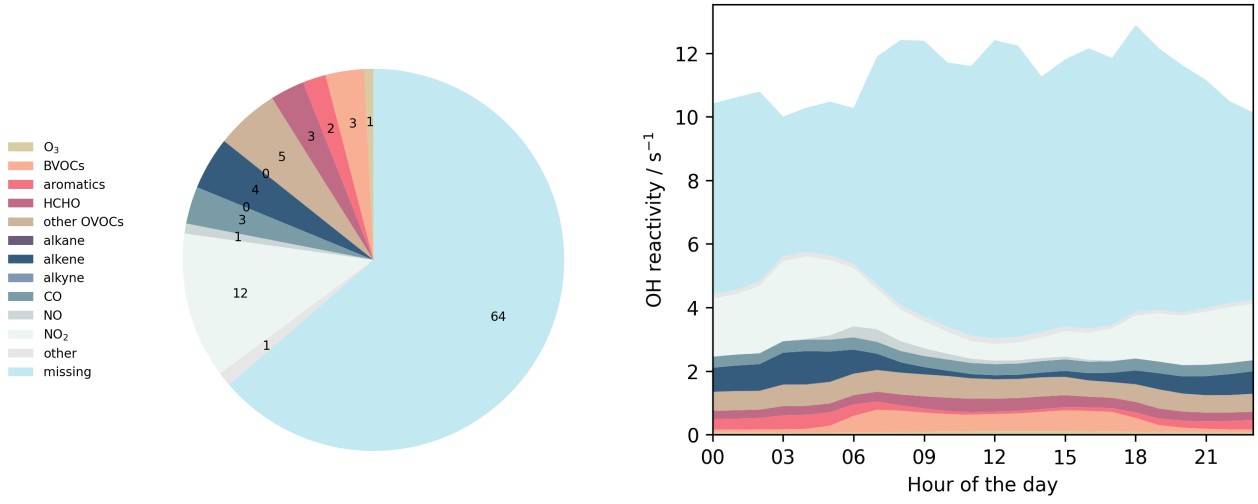

Figure S9. The breakdown in percentage and hourly diel averages of total OH reactivity by modeled trace species in 2017 field campaign.

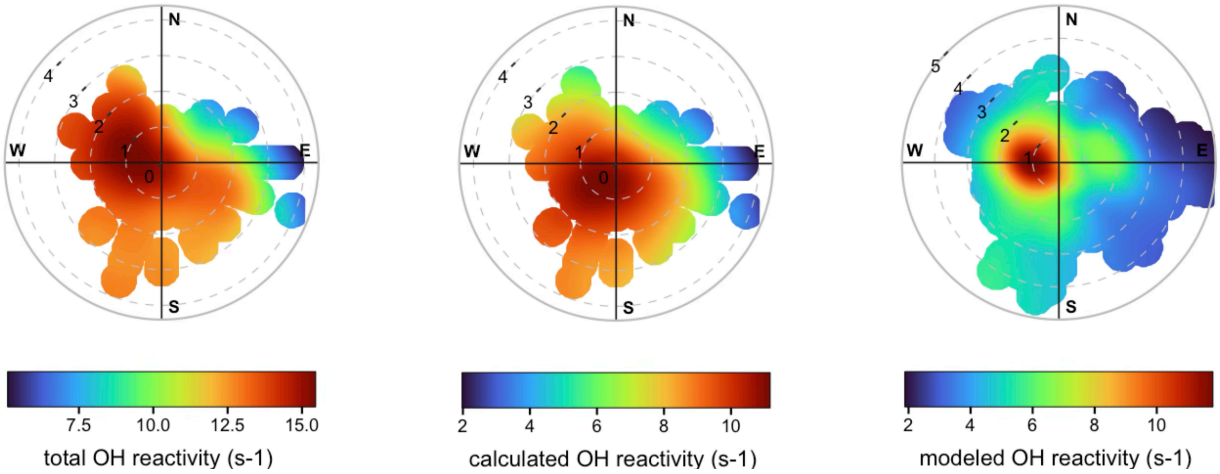

Figure S10. Bivariate polar plot of total OH reactivity (left), calculated OH reactivity from measured trace species (middle), and modeled OH reactivity (right) in 2017 Tsukuba campaign. The radial axis shows the wind speed in m s^{-1}. For left and middle panel, the monitored surface wind speed and wind direction were used; for right panel, the model output of 10-m wind speed and 10-m wind speed were used.

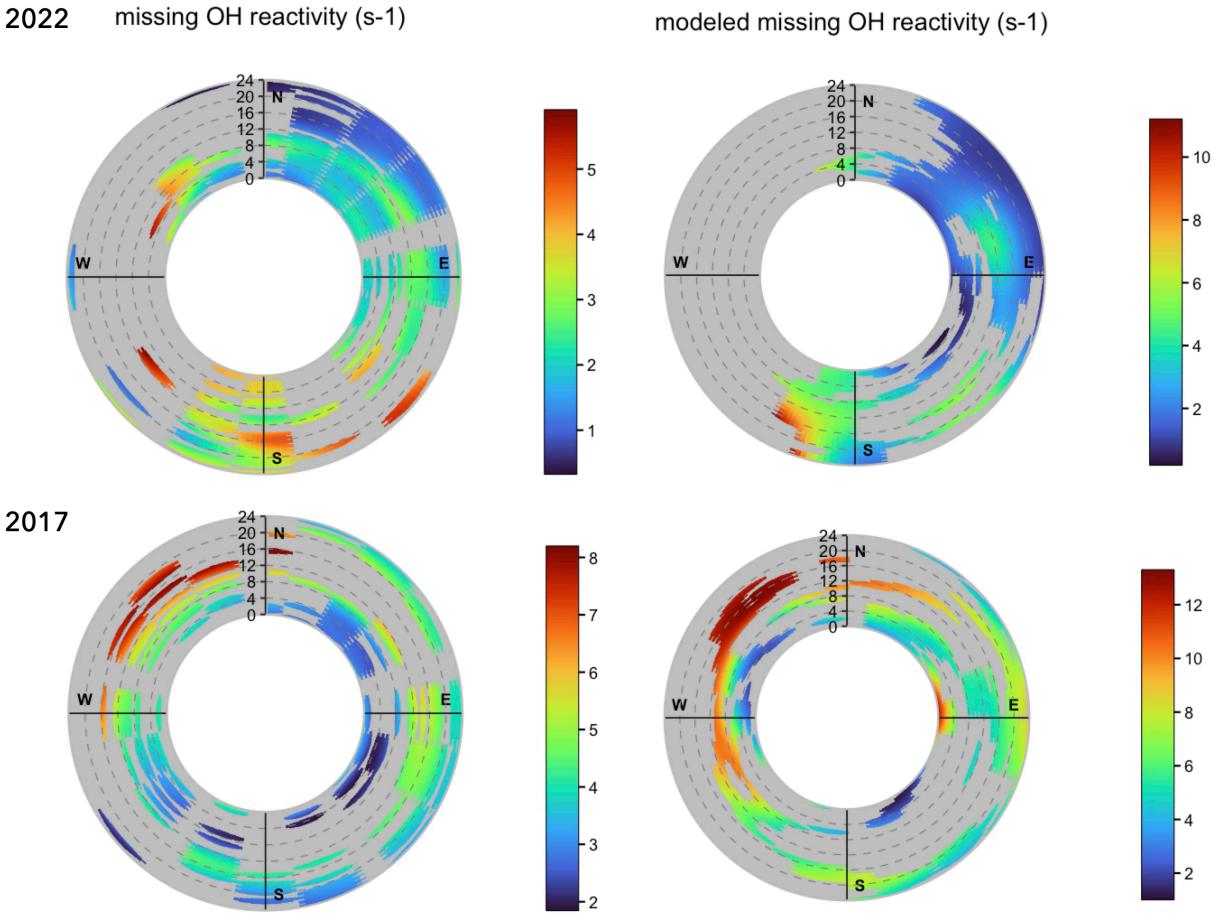

Figure S11. Diurnal variations of missing OH reactivity from bottom-up approach (in left) and model simulation (in right) in 2022 and 2017. Tbe radial axis shows the hour of the day. For left panel, the monitored surface wind speed and wind direction were used; for right panel, the model output of 10-m wind speed and 10-m wind speed were used.

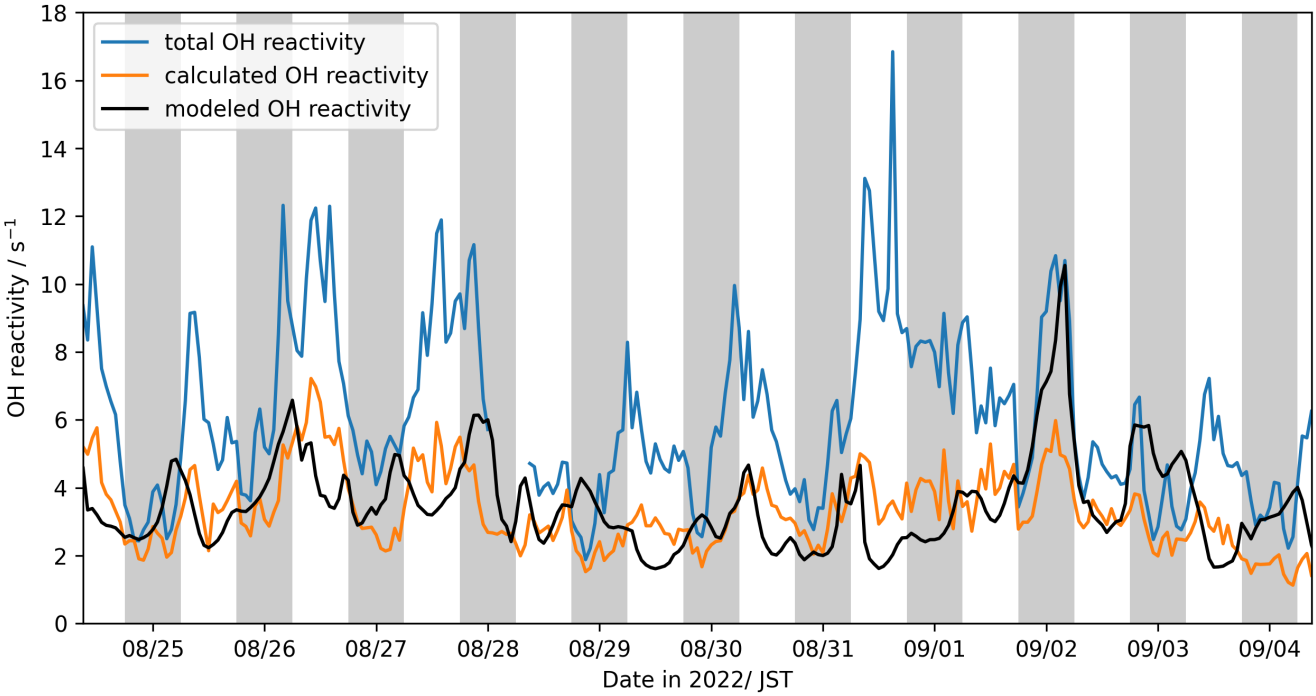

Figure S12. Time series of hourly total OH reactivity (in blue), calculated OH reactivity (in orange), and modeled OH reactivity (in black).

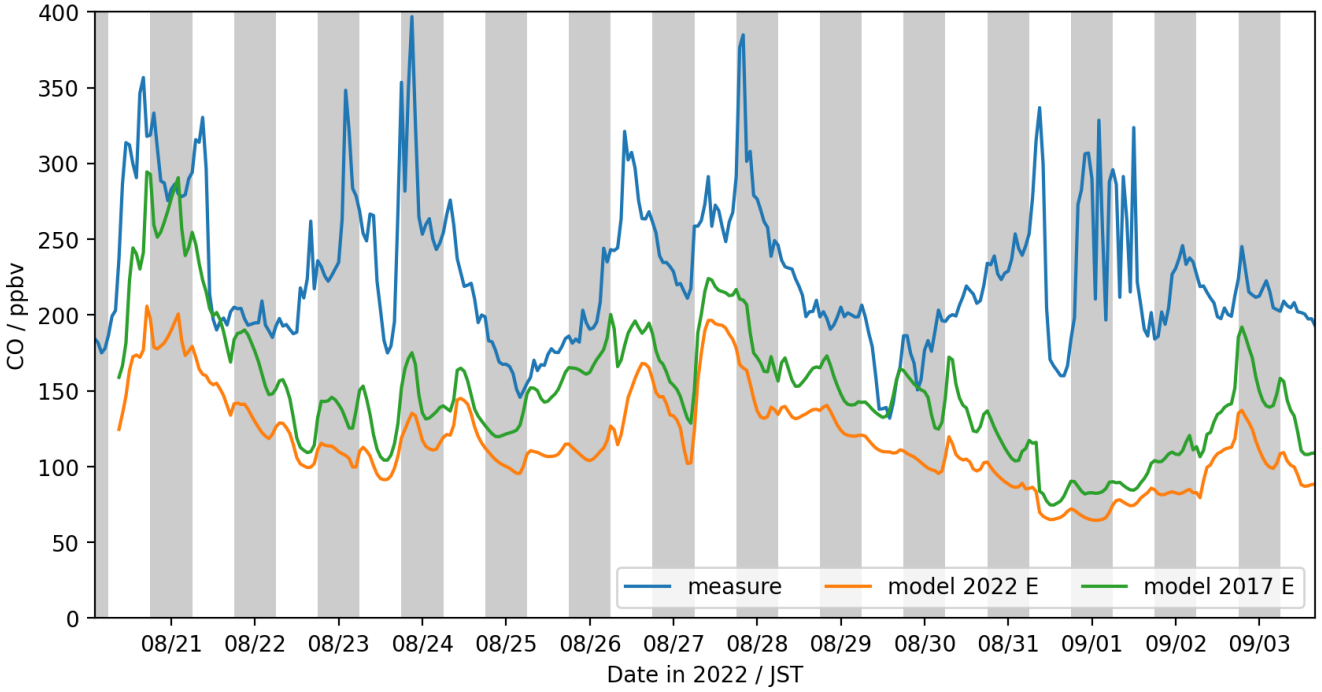

Figure S13. Time series of hourly CO concentration from measurements (in blue), simulation (in orange), and constrained simulation using 2017 emission inventories (in green).

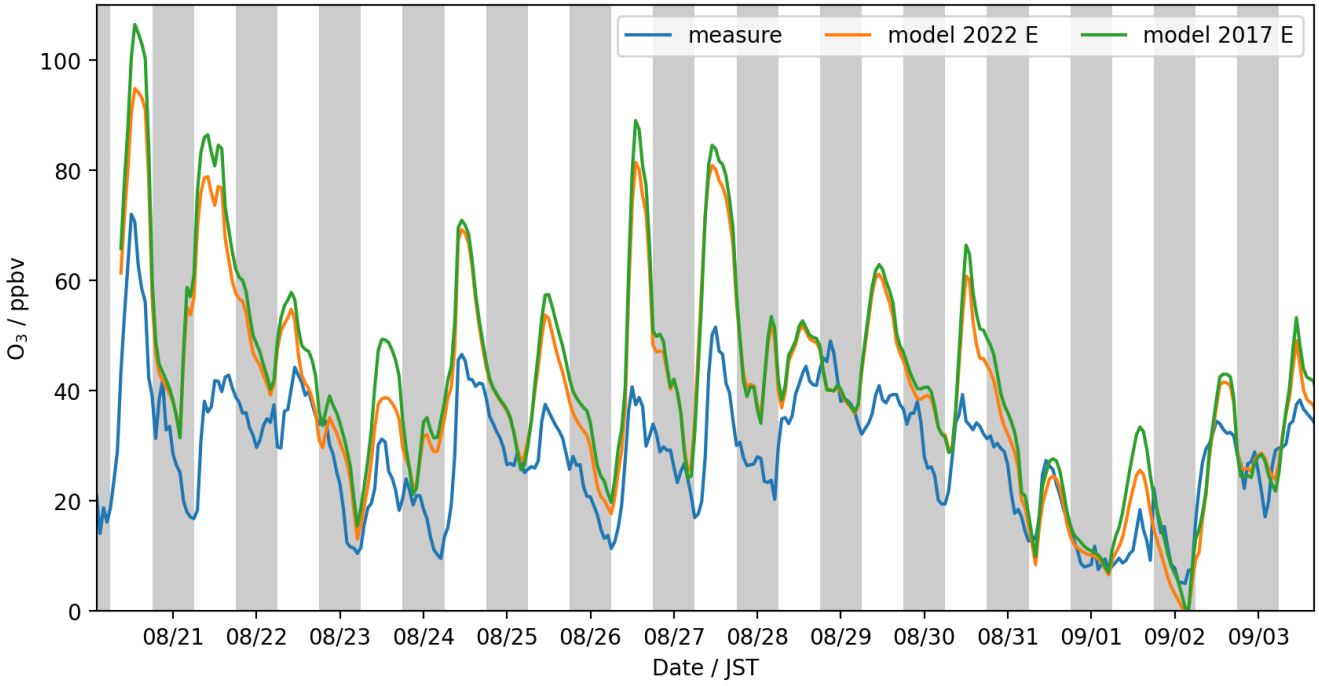
measure
model 2022 E
model 2017 E
O_3 / ppbv
0
20
40
60
80
100
08/21
08/22
08/23
08/24
08/25
08/26
08/27
08/28
08/29
08/30
08/31
09/01
09/02
09/03
Date / JST

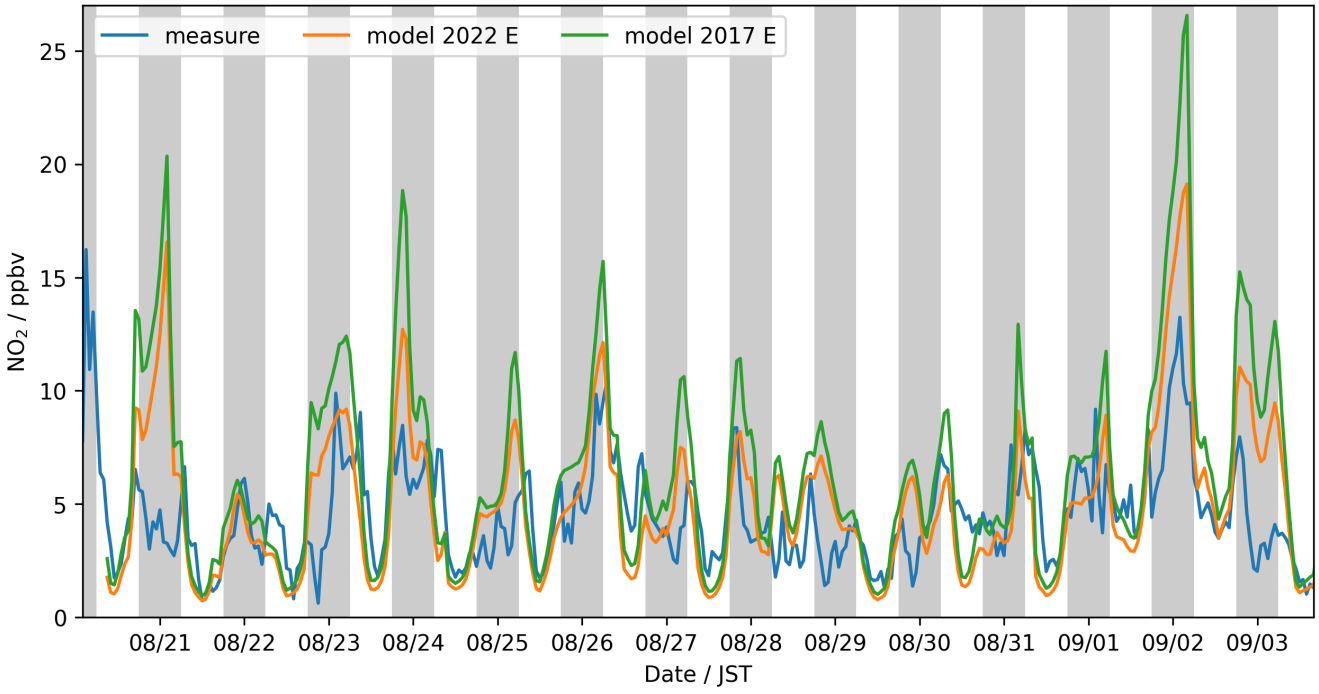
measure
model 2022 E
model 2017 E
NO_2 / ppbv
0
5
10
15
20
25
08/21
08/22
08/23
08/24
08/25
08/26
08/27
08/28
08/29
08/30
08/31
09/01
09/02
09/03
Date / JST

135

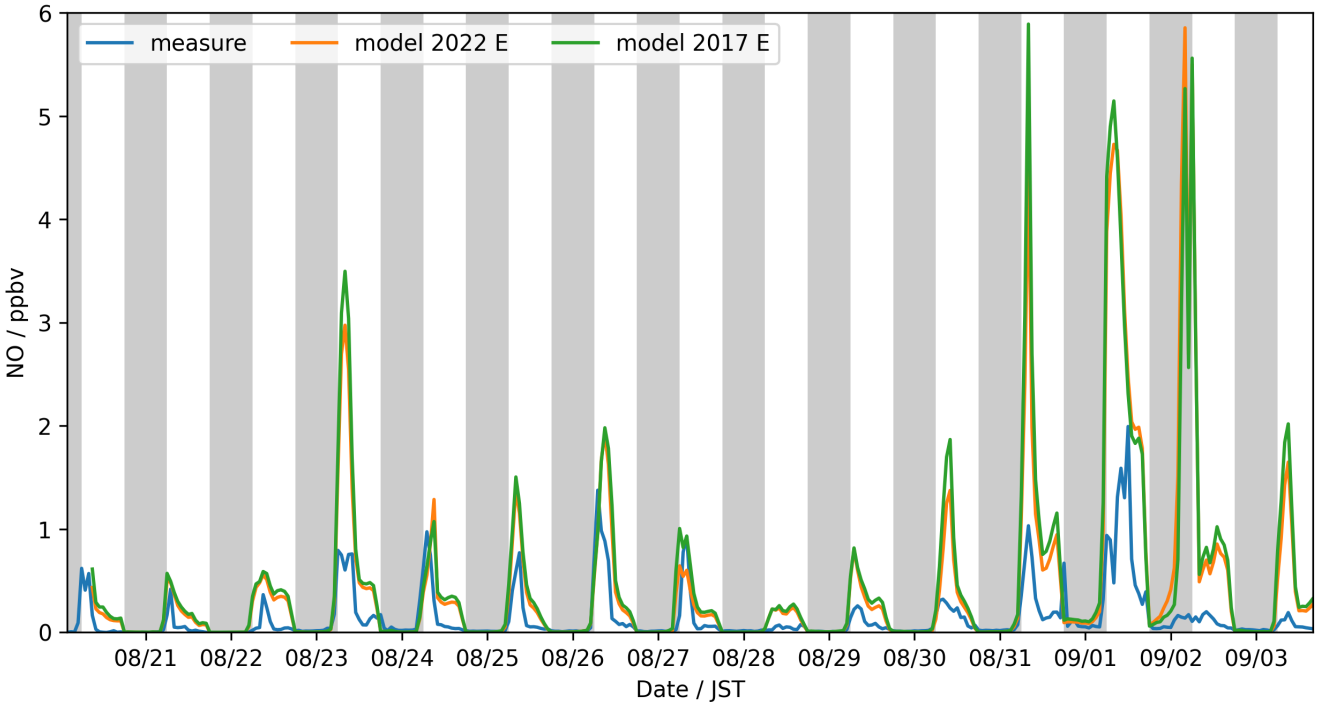

Figure S14. Time series of O_3 (upper panel), NO_2 (middle panel), and NO (bottom panel) from measurements (in blue), simulation (in orange), and constrained simulation using 2017 emission inventories (in green).

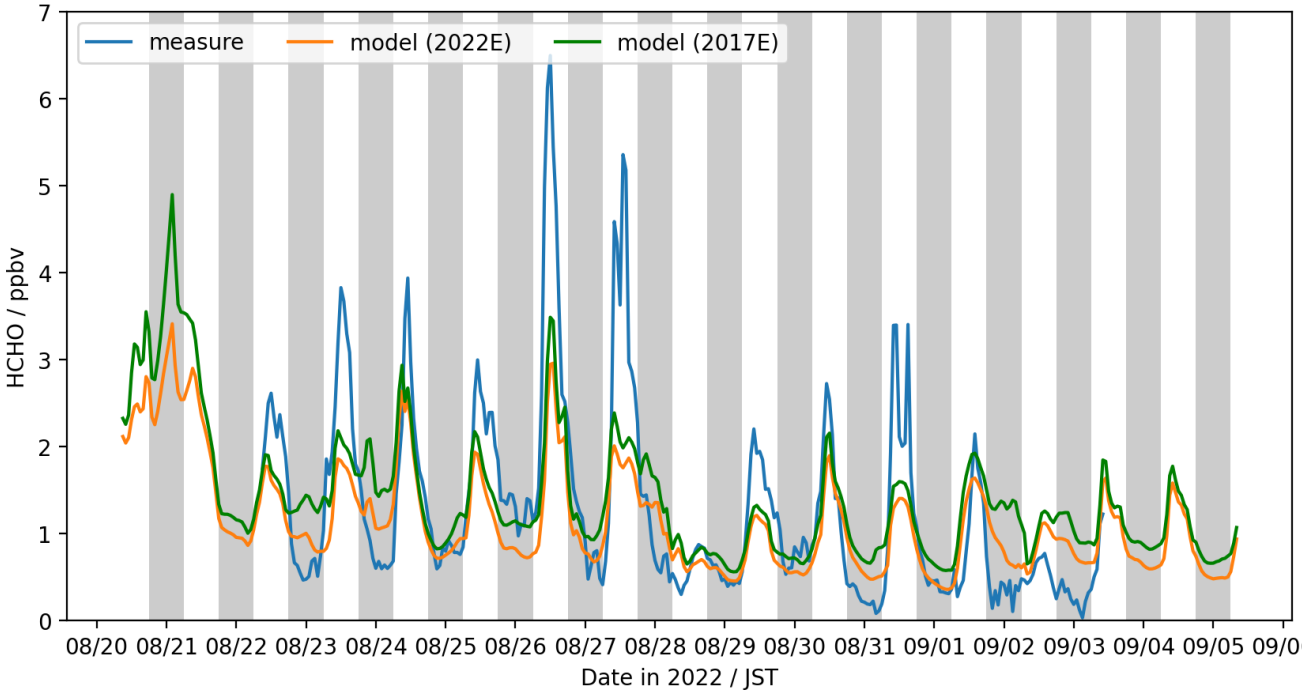

140

Figure S15. Time series of HCHO from measurements (in blue), simulation (in orange), and constrained simulation using 2017 emission inventories (in green).

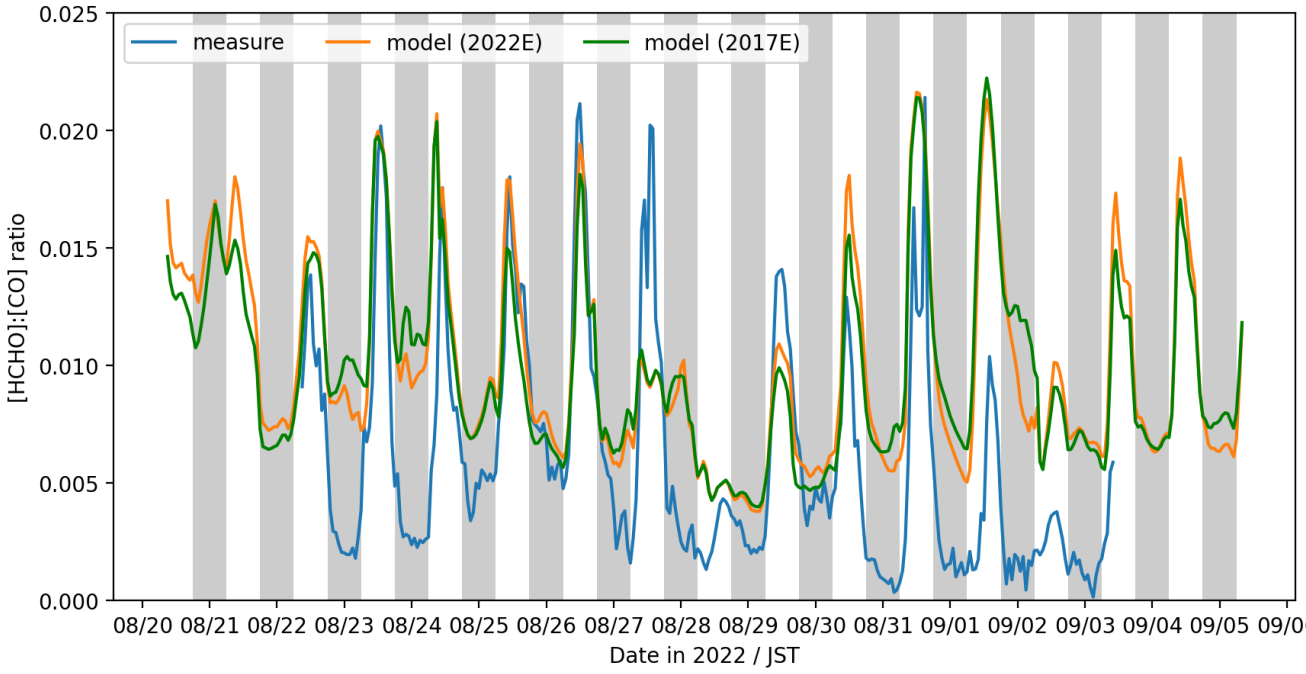

145

Figure S16. Time series of HCHO/CO ratio from measurements (in blue), simulation (in orange), and constrained simulation using 2017 emission inventories (in green).

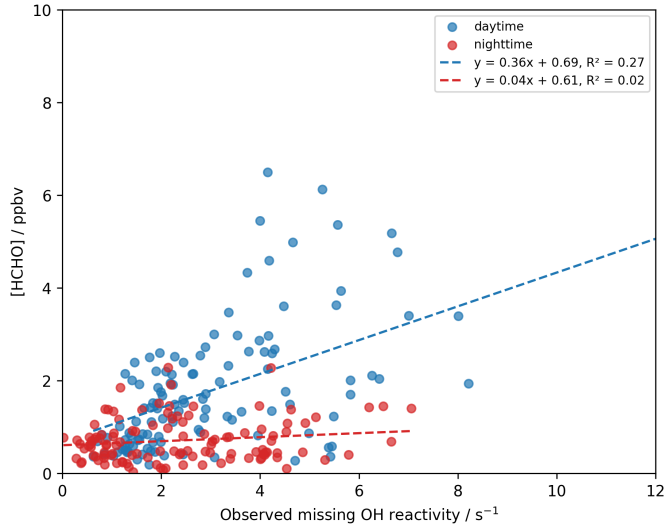

150 **Figure S17. Corresponding relationship between HCHO and observation-based missing OH reactivity compared in the daytime and nighttime.**

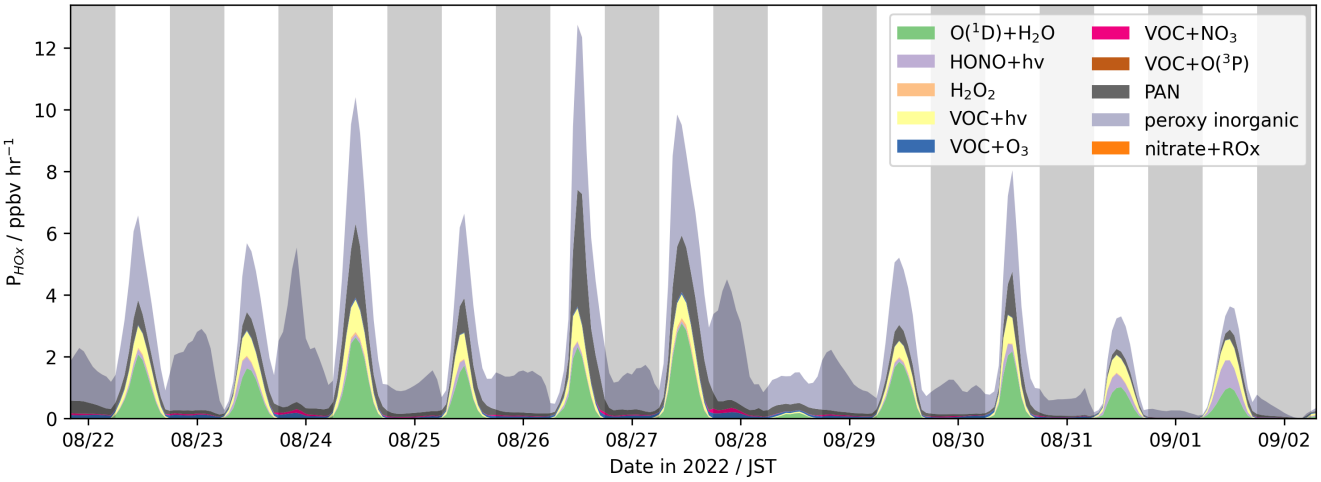

155

Figure S18. Time series of P(HOx) from the WRF- CMAQ model.

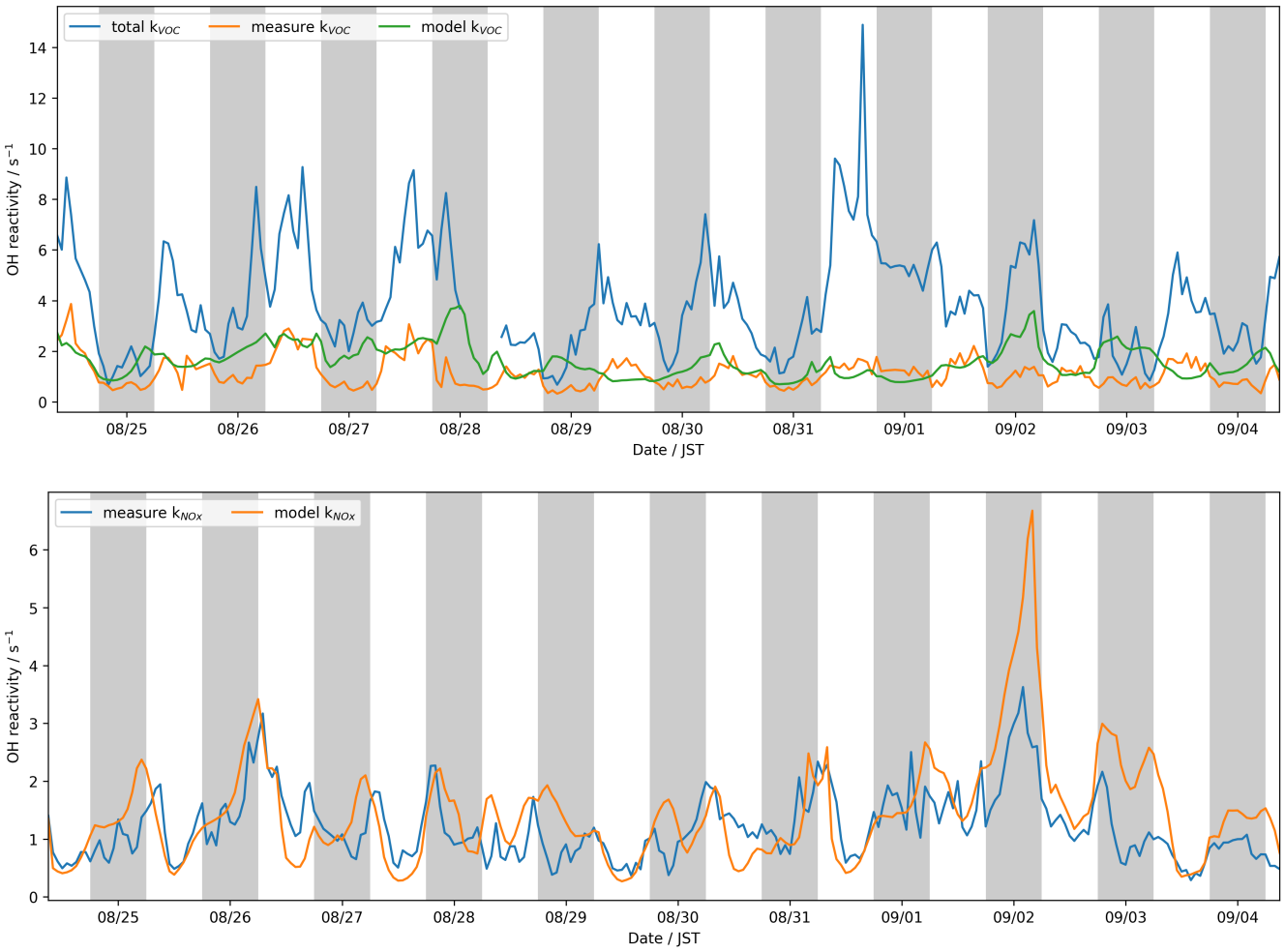

160

Figure S19. Upper panel: time series of VOC reactivity from top-down measurements (in blue), bottom-up measurements (in orange), and simulation (in green); lower panel: time series of NOx reactivity from measurements (in blue), and simulation (in orange).

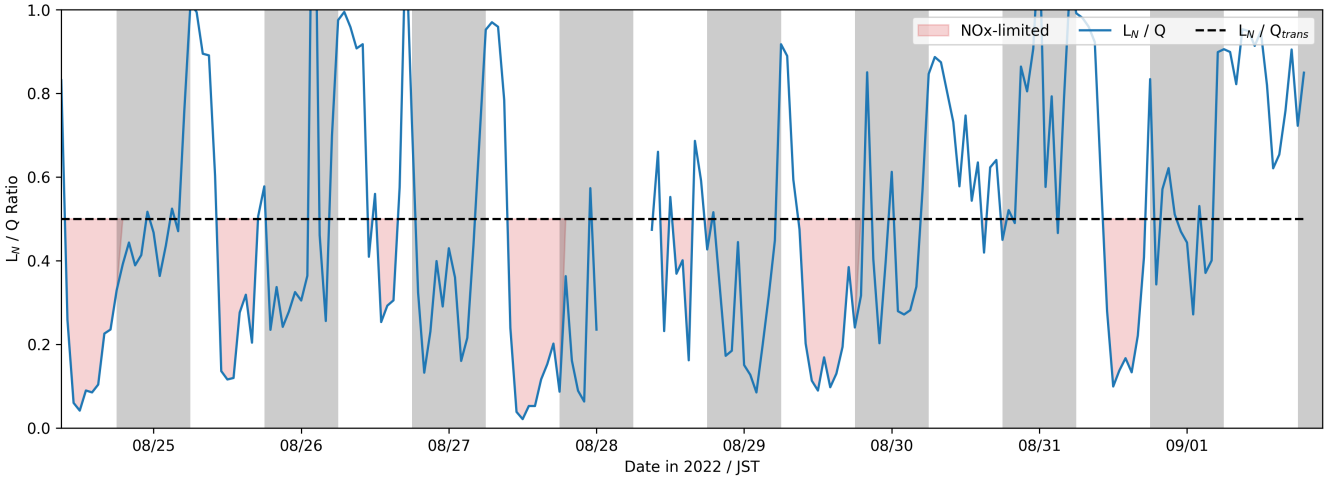

Figure S20. Ozone regime results from L_N/Q without considering the aerosol uptake effect.

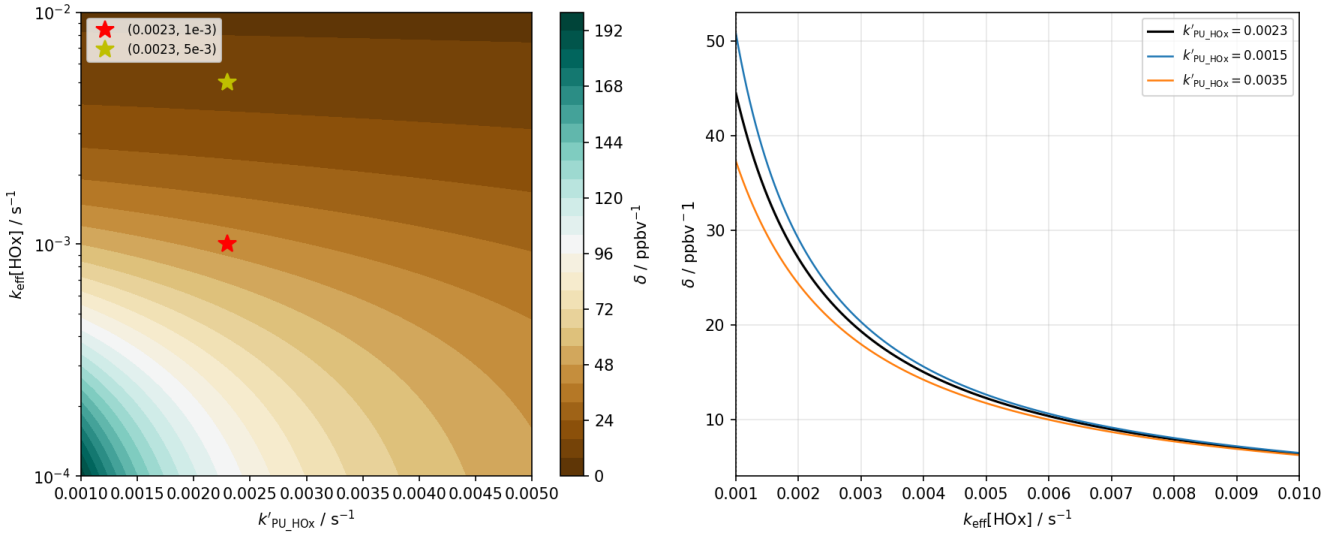

Figure S21. The δ sensitivity versus heterogeneous HOx loss rate and the gas-phase XO_2 self/cross-reaction loss rate. β is used as 0.67 and the $k_{HO2\text{-}NO}$ equals 8×10^{-12} cm^3 $molecule^{-1}s^{-1}$ in the sensitivity test.

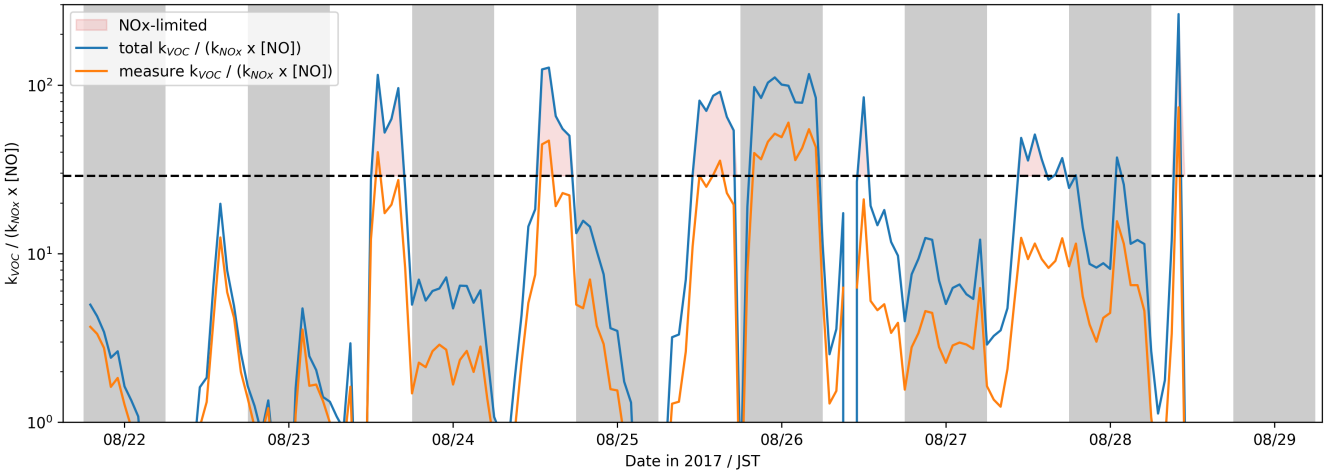

Figure S22. Ozone regime classification results using the empirical method proposed from k_{VOC}/k_{NOx} and [NO] relationship in 2017 Tsukuba campaign. The NOx-limited regime condition is highlighted in red. Dashed line indicates the transition regime where the y-value equals 28.9. For a cross-comparison of the results, the reader is recommended to refer to the Fig. 1 from Sakamoto et al. (2019).

References

Daranlot, J., Bergeat, A., Caralp, F., Caubet, P., Costes, M., Forst, W., Loison, J., and Hickson, K. M.: Gas-Phase Kinetics of Hydroxyl Radical Reactions with Alkenes: Experiment and Theory, ChemPhysChem, 11, 4002–4010, https://doi.org/10.1002/cphc.201000467, 2010.

Li, J., Sakamoto, Y., Kohno, N., Fujii, T., Matsuoka, K., Takemura, M., Zhou, J., Nakagawa, M., Murano, K., Sadanaga, Y., Nakashima, Y., Sato, K., Takami, A., Yoshino, A., Nakayama, T., Kato, S., and Kajii, Y.: Total hydroxyl radical reactivity measurements in a suburban area during AQUAS–Tsukuba campaign in summer 2017, Science of the Total Environment, 740, 139897, https://doi.org/10.1016/j.scitotenv.2020.139897, 2020.

Rubio, M. A., Lissi, E., Jorquera, H., Salinas, E., Castro, J., and Cádiz, M.: Carbon monoxide concentrations in Santiago City at street levels and their vertical gradient, Environ Monit Assess, 140, 161–173, https://doi.org/10.1007/s10661-007-9857-1, 2008.

Sakamoto, Y., Sadanaga, Y., Li, J., Matsuoka, K., Takemura, M., Fujii, T., Nakagawa, M., Kohno, N., Nakashima, Y., Sato, K., Nakayama, T., Kato, S., Takami, A., Yoshino, A., Murano, K., and Kajii, Y.: Relative and Absolute Sensitivity Analysis on Ozone Production in Tsukuba, a City in Japan, Environmental Science and Technology, 53, 13629–13635, https://doi.org/10.1021/acs.est.9b03542, 2019.

Sakamoto, Y., Egami, K., Li, J., Morino, Y., Nakashima, Y., Kato, S., Sato, K., Yoshino, A., Takami, A., Kohno, N., Sadanaga, Y., and Kajii, Y.: ROx budget analysis based on total OH reactivity and total ROx concentration measurements in Suburban Japan, Atmospheric Environment, 382, 122232, https://doi.org/10.1016/j.atmosenv.2026.122232, 2026.